Primer on Electroencephalography for Functional Connectivity

Thomas C Ferree[1] and Paul L Nunez[2]

[1] Department of Radiology and Bioengineering Graduate Group, University of California, San Francisco and Department of Radiology, University of Texas Southwestern Medical Center, Dallas
[2] Brain Physics, LLC and Department of Biomedical Engineering, Tulane University

1 Introduction

Experimental and theoretical studies of functional connectivity in healthy humans requires non-invasive techniques such as electroenchaphalography (EEG), magnetoencephalography (MEG), and functional magnetic resonance imaging (fMRI). Among these, EEG and MEG provide the most direct measure of cortical activity with high temporal resolution ($\lesssim$ 1 msec), but with spatial resolution (1–10 cm) limited by the locations of sensors on the scalp. In contrast, functional MRI has low temporal resolution (1–10 sec), but high spatial resolution (1–10 mm). To the extent that functional activity among brain regions in the cortex may be conceptualized as a large-scale brain network with diffuse nodes, fMRI may delineate the anatomy of these networks, perhaps most effectively in identifying major network hubs. Much current effort is aimed at the integration of these technologies and others, for the obvious reason: to provide the most complete view of dynamical brain activity both spatially and temporally. This chapter focuses primarily on EEG, but also makes connections with MEG.

The human brain exhibits interesting and relevant dynamics on all spatial scales, ranging from single neurons to the entire cortex. The spatial resolution of a particular measurement technique selects certain physiological processes over others. Much investigation in animals has focussed on the information capacities of single neurons, using direct measurements from implanted electrodes. Although EEG measurements integrate over the activity of 10–100 millions of neurons, there is ample evidence that relevant information is represented at these large scales. Indeed, interactions between remote brain areas must involve large spatial scales. Furthermore, several techniques have been

developed for improving the spatial resolution of scalp EEG so that dynamic behavior at the scale of roughly 2–3 cm may be estimated.

The physics and physiology of scalp EEG have been described at length elsewhere (Nunez 1981; Nunez 1995; Nunez and Srinivasan 2006). The goal of this chapter is partly to summarize that material, and partly to extend it. Section 2 describes the physiological genesis of EEG and MEG in terms of cellular currents. Section 3 describes the physical basis of EEG and MEG starting from Maxwell's equations. The remaining chapters focus exclusively on EEG. Section 4 shows how a multipole expansion of the electric potential defines the familiar current dipole. Section 5 adds the effects of head tissue inhomogeneities, which strongly affect the electric potential measured at the scalp. Section 6 reviews EEG measurement principles. Section 7 develops lead field theory, an intuitive way of thinking about the sensitivity of scalp electrodes to brain current sources. Together these sections link concepts of neural activity from the cellular level to the scalp, and provide a basis for the application of scalp EEG to study functional connectivity.

2 Biological Basis of EEG

2.1 Cortical Anatomy

The mammalian cortex is the outer mantle of cells surrounding the central structures, e.g., brainstem and thalamus. It is unique to mammals, and is believed to be necessary for most higher-level brain functions. Topologically the cortex is comprised of two spherical shells, corresponding to the two hemispheres. The hemispheres are connected by the corpus callosum. Cortical thickness varies mostly between 2–3 mm in the human, and is folded around the subcortical structures so as to appear wrinkled. Its average surface area is about 2200 cm^2 (Zilles 1990).

It is estimated that there are roughly 10^{11} neurons in the human brain, and 10^{10} of these in the cortex. Of these, approximately 85% are pyramidal cells (Braitenberg and Schuz 1991), whose dendritic trees have a distinctive, elongated geometry that makes possible the generation of extracellular fields at large distances. The remaining 15% may be broadly classified as stellate cells, whose dendritic trees are approximately spherical, and make little or no contribution to distant fields. Of course, both cells types are interconnected to form a single dynamical network, but it is believed that the fields at large distances are dominated by pyramidal cells.

Synaptic connections in the cortex are dense. Each cortical neuron receives 10^4–10^5 synaptic connections, with most inputs coming from distinct neurons. Pyramidal cells make excitatory connections to both cell types. They make intracortical connections over lengths ranging 0.5–3 mm, and cortico-cortical connections over lengths ranging 1–20 cm. Stellate cells make inhibitory connections to both cell types. They make intracortical connections over lengths

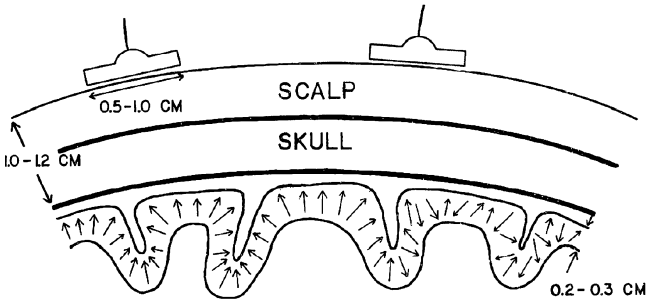

Fig. 1. Depiction of the human head, and the positioning of EEG electrodes relative to the folded cortex. Adapted from Nunez (1995).

ranging only 0.02–0.03 mm. Thus connections in the cortex are said to exhibit long-range excitation and short-range inhibition. Because of the diversity of scales of these synaptic connections, and the nonlocal nature of the cortico-cortical connections, we expect the cortex to exhibit rich spatio-temporal dynamics spanning a wide range of length and time scales.

Figure 1 shows a depiction of several layers of the human head and the positioning of EEG electrodes relative to the cortex. The folds of the cortex are such that even nearby patches of cortex can have different orientations and distances from the detectors. Section 6 shows how individual EEG and MEG detectors spatially integrate neural activity over as much as 100 cm^2. Combining the data from many scalp probes, however, yields an improvement to the order of several cm^2. Using the latter estimate, we must still conclude that EEG and MEG detectors integrate brain activity over a volume including as many as 10^7–10^9 cortical neurons.

2.2 Neurons and Synapses

Neurons are highly specialized for signal processing and conduction via electrochemical processes. The morphological structure of a neuron includes a cell body, called the soma, and elaborate branching structures that enable communication with sensory receptors, distant neurons, etc. In the simplest view, input and output are handled separately. Inputs are collected in a continuous fashion by the dendrites, and represented as a variation of the transmembrane voltage. Multiple inputs are summed in the dendritic tree, and the net input is represented as transmembrane voltage at the soma. When the soma voltage reaches some threshold, a discrete voltage pulse is generated, called an action potential, which propagates down the axon as output. The end of the axon also has elaborate branching to enable communication with target neurons. The input-output properties of neurons have been studied extensively and modeled in detail (Koch and Segev 1989).

2.3 Neuronal Currents

In biological tissues, there are no free electrons. Electric currents are due to ions, e.g., K^+, Na^+, Cl^-, Ca^{2+}, etc. These ions flow in response to the local electric field, according to Ohm's law, but also in response to their local concentration gradient, according to Fick's law (Plonsey 1969). In the resting state of the membrane, the concentration gradients and electric field are due to ion channel pumps, which use energy acquired from ATP to move ions across the membrane against their diffusion gradient.

The concentration of each ion inside and outside the membrane remains essentially constant in time. The transmembrane voltage, however, changes radically in time, the strongest example being the action potential. Thus for the purposes of discussing small scale neural activity, we take the transmembrane potential V_m as the primary dynamic state variable to be considered. By convention, V_m is defined as the potential inside relative to that outside, i.e., $V_\mathrm{m} = V_\mathrm{i} - V_\mathrm{o}$. The current per unit length i_m flowing across the membrane, rather than the transmembrane potential, is considered the basic source variable of the extracellular fields detected by EEG and MEG.

Currents flow in neurons when a neurotransmitter binds to receptors on ion channels located in the membrane. Detailed consideration of a three-dimensional dendrite or axon has shown that the phenomenon of current flow in the cell may be well described by a one-dimensional approximation. The same mathematical treatment applies to undersea telegraph cables, comprised of an insulated metal core immersed in conductive salt water, thus the treatment is called "cable theory."

Assuming a membrane with conductive and capacitive properties, surrounded by fluids with conductive properties only, and applying current conservation in each compartment leads to

$$\tau_\mathrm{m} \frac{\partial V_\mathrm{m}}{\partial t} = \lambda_\mathrm{m}^2 \frac{\partial^2 V_\mathrm{m}}{\partial x^2} - (V_\mathrm{m} - E_\mathrm{r}) - r_\mathrm{m}\, i_\mathrm{other}(x,t) \tag{2.1}$$

where the membrane time constant $\tau_\mathrm{m} = r_\mathrm{m} c_\mathrm{m}$, the neuron space constant $\lambda_\mathrm{m} = \sqrt{r_\mathrm{m}/(r_\mathrm{i} + r_\mathrm{o})}$, the membrane resistance times unit area $r_\mathrm{m} = 1/g_\mathrm{m}$, and E_r is the resting transmembrane potential. Mathematically this is identical in form to the heat equation, which governs the one-dimensional flow of heat in a heat-conducting rod. It has been studied extensively and has well-known analytic solutions for appropriate boundary conditions.

Consider an isolated dendrite of length L, with current injected at one end. A solution may be derived for $V_m(x)$. The corresponding transmembrane current per unit length $i_m(x)$ may be written

$$i_\mathrm{m}(x) \simeq -I_0\ \delta(x) + \sqrt{\frac{r_\mathrm{i}}{r_\mathrm{m}}} I_\mathrm{inj}\ \mathrm{e}^{-x/\lambda_\mathrm{m}}, \qquad x \geq 0 \tag{2.2}$$

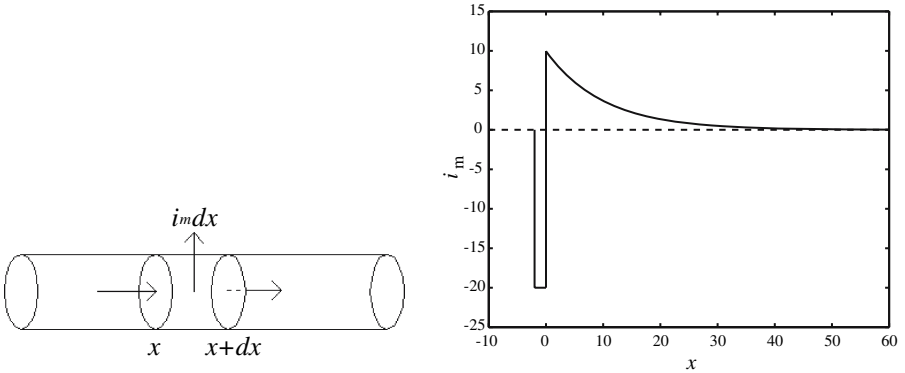

Fig. 2. (**a**) Cylindrical cable representing a segment of dendrite or axon. A single compartment is shown with transmembrane current per unit length i_m. (**b**) Transmembrane current per unit length i_m at steady-state, due to current injected at $x = 0$. (The delta function at $x = 0$ is not drawn to scale; the actual area of the delta function equals the area of the positive (outward) current flow.)

where $\delta(x)$ is the Dirac delta function. Figure 2(b) shows the solution for $x \geq 0$. The delta function in Fig. 2(b) is not drawn to scale; the integral of (2.2) over all x is zero. Section 4 shows that, far away from the cable, the potential Φ may be approximated as if it were generated by an ideal dipole, consisting of a point source and sink separated by a distance λ_m. This transmembrane current, driven not so much by the transmembrane potential as by difffusion, implies a nonzero extracellular electric field through current conservation.

2.4 Large Neural Populations

Neuronal currents of this sort generate extracellular electric and magnetic fields, which are detected using EEG and MEG. The fields generated by a single neuron are much too small to be detected at the scalp, but the fields generated by synchronously active neurons, with advantageous geometric alignment, can be detected. Stellate cells have approximately spherical dendritic trees, so far away the extracellular fields tend to add with all possible orientiations and cancel. Pyramidal cells have similar dendritic trees, but the tree branches are connected to the cell body (soma) by a long trunk, called the apical dendrite. It is a fortuitous anatomical feature of the cortex that pyramidal cells have their apical dendrites aligned systematically, along the local normal to the cortical surface. In this way, the fields of pyramidal neurons superimpose geometrically to be measurable at the scalp.

Several factors contribute to the net fields measured at the scalp. Many active neurons and fortuitous alignment are not enough. As neuronal oscillations tend to oscillate with predominant frequencies, dependent upon functional activity, only synchronously active neurons will sum coherently in time (Elul 1972; Nunez 1981). Consider a 1 cm^2 region of cortex, containing approximately 10^7 aligned pyramidal cells. Make the idealized assumption that all these neurons are oscillating at the predominant frequency, (e.g., 10 Hz resting rhythm). If only 1% of these neurons are synchronously active, i.e., oscillate in phase with each other, and 99% are oscillating with random phase. If the contribution from the asynchronous neurons may be treated as Gaussian then, because N unit-variance Gaussian random numbers sum to $\sqrt{N}$, the relative contribution of synchronous to asynchronous neurons would be $10^5/\sqrt{10^7} \simeq 30$. Thus scalp EEG and MEG are considered to be dominated by synchronous neural activity. Indeed, amplitude reduction in EEG clinical and research circles is often termed desynchronization. Of course, phase desynchronization is only one of many possible mechanisms that could reduce the amplitude of the net voltage at the scalp. Alternatively, synchronous spike input to a patch of cortex can generate event-related synchronization in the dendritic fields. Such phase synchronization is one mechanism for producing event-related potentials (Makeig et al. 2002).

3 Physical Basis of EEG

3.1 Electromagnetic Fields in Conductive Media

The physics of electric and magnetic fields in matter is summarized by Maxwell's equations. This set of coupled, linear equations has source terms given by the charge density ρ and the current density $\mathbf{J}$. Additional contributions arise from the time derivatives of the fields. In matter the macroscopic fields obey (Jackson 1975)

$$\vec{\nabla} \cdot \mathbf{D} = \rho \tag{3.1}$$

$$\vec{\nabla} \cdot \mathbf{B} = 0 \tag{3.2}$$

$$\vec{\nabla} \times \mathbf{E} = -\frac{\partial \mathbf{B}}{\partial t} \tag{3.3}$$

$$\vec{\nabla} \times \mathbf{H} = \mathbf{J} + \frac{\partial \mathbf{D}}{\partial t} \tag{3.4}$$

where $\mathbf{E}$ is called the electric field, and H is called the magnetic field[3]. The electric displacement $\mathbf{D}$ is related to the electric field $\mathbf{E}$ through ϵ the dielectric constant: $\mathbf{D} = \epsilon\mathbf{E}$. The magnetic induction $\mathbf{B}$ is related to the electric field $\mathbf{H}$ through μ the magnetic susceptibility: $\mathbf{B} = \mu\mathbf{H}$.

[3] Here Maxwell's equations are expressed in MKS units. The equations appear different from those in CGS units (Jackson 1975), but MKS is the more common in bioelectromagnetism (Gulrajani 1998).

Maxwell's equations reflect the basic principle of charge conservation. Taking the divergence of (3.4) and the time derivative of (3.1) leads to

$$\vec{\nabla} \cdot \mathbf{J} + \frac{\partial \rho}{\partial t} = 0 \tag{3.5}$$

Integrating over a closed volume V bounded by a surface S and using the divergence theorem (Arfken 1995) shows that the component of the current flowing outward across S equals minus the time rate of change of the charge in the volume bounded by S.

3.2 Macroscopic Source Current J_S

Biological tissues have conductive and capacitive properties, but the magnetic susceptibility is essentially that of vacuum. In metals the charge carriers are free electrons, but in biological tissue the charge carriers are ions, e.g., Na^+, K^+, Cl^-, Ca^{2+}, etc. Section 2 described how the membrane current density $\mathbf{J}$ has both electric and diffusive contributions. In the extracellular space, the story is more complicated. There is no concentration gradient or diffusive contribution *per se*, nevertheless, the fields in the extracellular space may be computed by considering the current density to have two contributions:

$$\begin{aligned} \mathbf{J} &= \mathbf{J}_\mathrm{E} + \mathbf{J}_\mathrm{S} \\ &= \sigma \mathbf{E} + \mathbf{J}_\mathrm{S} \end{aligned} \tag{3.6}$$

where $\mathbf{J}_\mathrm{E}$ is the *ohmic* current that flows in response to the local electric field, and $\mathbf{J}_\mathrm{S}$ is the *source* current (or *impressed* current). Within the membrane, (2.1) includes contributions to the current arising from both the transmembrane electric field and the transmembrane concentration gradients for each ion species. For computing fields in the extracellular space, $\mathbf{J}_\mathrm{S}$ is a phenomenological device that subsumes other physical aspects of the problem (Plonsey 1982; Nunez and Srinivasan 2006).

3.3 Solution to Maxwell's Equations

Maxwell's equations may be solved analytically if the parameters ϵ, μ, and σ are constant in space. This ideal case forms the basis of solutions in systems with piecewise constant parameters. The solution to (3.1–3.4) for the fields $\mathbf{E}$ and $\mathbf{B}$ is obtained by introducing the magnetic (vector) potential $\mathbf{A}$, defined by

$$\mathbf{B} = \vec{\nabla} \times \mathbf{A} \tag{3.7}$$

and the electric (scalar) potential Φ, defined by

$$\mathbf{E} = -\vec{\nabla}\Phi - \frac{\partial \mathbf{A}}{\partial t} \tag{3.8}$$

Because these equations involve the curl of $\mathbf{A}$ and the divergence of Φ, and there are vector identities specifying the conditions in which the divergence and curl vanish, there is additional flexibility in defining these potentials. This flexibility is called gauge invariance, and by choosing a convenient gauge:

$$\vec{\nabla} \cdot \mathbf{A} + \mu\epsilon \frac{\partial \Phi}{\partial t} + \mu\sigma\Phi = 0 \tag{3.9}$$

the differential equations for $\mathbf{A}$ and Φ separate (Gulrajani 1998).

Assuming harmonic time dependence $\Phi(\mathbf{r}, t) = \mathrm{Re}[\tilde{\Phi}(\omega, t)\mathrm{e}^{i\omega t}]$, the uncoupled equations have the well-known solutions (Arfken 1995).

$$\tilde{\Phi}(\mathbf{r}, \omega) = \frac{-1}{4\pi(\sigma + i\omega\epsilon)} \int_{\mathrm{V}} \frac{\vec{\nabla}' \cdot \tilde{\mathbf{J}}_{\mathrm{S}}(\mathbf{r}', \omega)}{|\mathbf{r} - \mathbf{r}'|} \, \mathrm{e}^{-ik|\mathbf{r}-\mathbf{r}'|} \, d^3r' \tag{3.10}$$

and

$$\tilde{\mathbf{A}}(\mathbf{r}, \omega) = \frac{\mu}{4\pi} \int_{\mathrm{V}} \frac{\tilde{\mathbf{J}}_{\mathrm{S}}(\mathbf{r}', \omega)}{|\mathbf{r} - \mathbf{r}'|} \, \mathrm{e}^{-ik|\mathbf{r}-\mathbf{r}'|} \, d^3r' \tag{3.11}$$

These solutions are valid at any frequency, and are therefore useful in electrical impedance tomography (EIT) and transcranial magnetic stimulation (TMS), where the electric and magnetic fields are controlled by an external device that may be driven to high frequencies, e.g., ∼100kHz. When applied to EEG and MEG, however, where the frequencies are limited physiologically, these equations may be simplified by the approximation $\omega \to 0$. This is called the quasi-static limit: the fields at each time point t are computed from the sources at that same time point, with no electromagnetic coupling or propagation delays related to the speed of light.

3.4 Quasistatic Formulation

Electric Potential

The solutions for Φ and $\mathbf{A}$ may be derived more directly by taking the quasistatic limit at the start, i.e., setting all time derivatives in Maxwell's equations equal to zero. The differential statement of current conservation (3.5) becomes

$$0 = \vec{\nabla} \cdot \mathbf{J} = \vec{\nabla} \cdot \mathbf{J}_{\mathrm{E}} + \vec{\nabla} \cdot \mathbf{J}_{\mathrm{S}} \tag{3.12}$$

Substituting $\mathbf{E} = -\vec{\nabla}\Phi$ leads to

$$\vec{\nabla} \cdot (\sigma \vec{\nabla} \Phi) = \vec{\nabla} \cdot \mathbf{J}_{\mathrm{S}} \tag{3.13}$$

Assuming σ is constant reduces this to Poisson's equation

$$\nabla^2 \Phi = \frac{1}{\sigma} \vec{\nabla} \cdot \mathbf{J}_{\mathrm{S}} \tag{3.14}$$

which has the well-known solution

$$\Phi(\mathbf{r},t) = \frac{-1}{4\pi\sigma}\int_{\mathrm{V}} \frac{\vec{\nabla}' \cdot \mathbf{J}_{\mathrm{S}}(\mathbf{r}',t)}{|\mathbf{r}-\mathbf{r}'|}\, d^3r' \tag{3.15}$$

Thus the electric potential Φ may be computed at each time point t as though $\mathbf{J}_{\mathrm{S}}$ were constant in time.

Magnetic Field

Similarly, for the magnetic field,

$$\nabla^2\mathbf{B} = -\mu_0\vec{\nabla}\times\mathbf{J} \tag{3.16}$$

Assuming σ is constant reduces this to a simpler expression in terms of the source current $\mathbf{J}_{\mathrm{S}}$ only

$$\nabla^2\mathbf{B} = -\mu_0\vec{\nabla}\times\mathbf{J}_{\mathrm{S}} \tag{3.17}$$

This is Poisson's equation for each component of $\mathbf{B}$, and has the solution

$$\mathbf{B}(\mathbf{r},t) = \frac{\mu_0}{4\pi}\int_{\mathrm{V}} \frac{\vec{\nabla}' \times \mathbf{J}_{\mathrm{S}}(\mathbf{r}',t)}{|\mathbf{r}-\mathbf{r}'|}\, d^3r' \tag{3.18}$$

The fundamental similarity between electric and magnetic fields, even when uncoupled at low frequencies, leads to parallel expressions of the basic EEG and MEG equations.

4 Dipole Source Modeling

4.1 Multipole Expansion of Φ

Equations (3.15) and (3.18) are the general solutions for Φ and $\mathbf{B}$ given an arbitrary current source density $\mathbf{J}_{\mathrm{S}}$ in the absence of boundaries. The integrand of each function involves derivatives of $\mathbf{J}_{\mathrm{S}}(\mathbf{r}')$, and the integration kernel $1/|\mathbf{r}-\mathbf{r}'|$ called the Green's function (Jackson 1975). The basis of the multipole expansion is to assume that $\mathbf{J}_{\mathrm{S}}(\mathbf{r}')$ is confined to some finite region of space, and that the point $\mathbf{r}$ at which the field is being computed or measured is far away compared to the size of the source distribution, i.e., $|\mathbf{r}| \gg |\mathbf{r}'|$. Computing the Taylor series of $1/|\mathbf{r}-\mathbf{r}'|$ through the first two terms gives

$$\frac{1}{|\mathbf{r}-\mathbf{r}'|} = \frac{1}{|\mathbf{r}|} + \frac{\mathbf{r}\cdot\mathbf{r}'}{|\mathbf{r}|^3} + \frac{1}{2}\sum_{i=1}^{3}\sum_{j=1}^{3}\frac{3r_ir_j - \delta_{ij}|\mathbf{r}|^2}{|\mathbf{r}|^5}r_i'r_j' + \ldots, \quad |\mathbf{r}'| \ll |\mathbf{r}| \tag{4.1}$$

The first term is called the *monopole* term, and falls off as $1/|\mathbf{r}|$. The second term is called the *dipole* term, and falls off as $1/|\mathbf{r}|^2$. The third term is called

the quadrupole term, and falls off as $1/|\mathbf{r}|^3$, and so on. Inserting (4.1) into (3.15) gives

$$\Phi(\mathbf{r}) = \Phi^{(1)}(\mathbf{r}) + \Phi^{(2)}(\mathbf{r}) + \Phi^{(3)}(\mathbf{r}) + \dots \tag{4.2}$$

and so on.

The monopole term is

$$\begin{aligned} \Phi^{(1)}(\mathbf{r}) &= \frac{-1}{4\pi\sigma}\frac{1}{|\mathbf{r}|}\int_V \vec{\nabla}' \cdot \mathbf{J}_{\mathrm{S}}(\mathbf{r}')\, d^3r' \\ &= \frac{-1}{4\pi\sigma}\frac{1}{|\mathbf{r}|}\int_S \mathbf{J}_{\mathrm{S}}(\mathbf{r}') \cdot \hat{\mathbf{n}}\, dS' \end{aligned} \tag{4.3}$$

where the second equality follows from the divergence theorem. If the volume V contains as many source as sinks (of equal strength), then the monopole term vanishes by current conservation.

The dipole term is

$$\begin{aligned} \Phi^{(2)}(\mathbf{r}) &= \frac{1}{4\pi\sigma}\left[\int_V \mathbf{r}'\left(\vec{\nabla}' \cdot \mathbf{J}_{\mathrm{S}}(\mathbf{r}')\right) d^3r'\right] \cdot \vec{\nabla}\frac{1}{|\mathbf{r}|} \\ &= \frac{1}{4\pi\sigma}\, \mathbf{p} \cdot \vec{\nabla}\frac{1}{|\mathbf{r}|} \end{aligned} \tag{4.4}$$

where the *dipole moment* is defined as

$$\mathbf{p} = \int \mathbf{r}'\left(\vec{\nabla}' \cdot \mathbf{J}_{\mathrm{S}}(\mathbf{r}')\right) d^3r' \tag{4.5}$$

Because the monopole term normally vanishes, and the quadrupole term falls off more quickly with distance, the dipole term usually makes the largest contribution to Φ and $\mathbf{B}$.

4.2 Electric Dipoles

Point Sources

A current dipole may be idealized as a source and sink with equal magnitude, separated by an infinitesimal distance d. This may be written formally as

$$\vec{\nabla} \cdot \mathbf{J}_{\mathrm{S}} = -I_0 \lim_{d\to 0}\left[\delta^{(3)}(\mathbf{r}-\mathbf{r}_+) - \delta^{(3)}(\mathbf{r}-\mathbf{r}_-)\right] \tag{4.6}$$

where $\mathbf{r}_+$ ($\mathbf{r}_-$) is the source (sink) location, and $\mathbf{d} \equiv \mathbf{r}_- - \mathbf{r}_+$ is the directed distance from sink to source.[4] Inserting (4.6) into (4.5) leads to an intuitive expression for the dipole moment:

$$\mathbf{p} = I_0\mathbf{d} \tag{4.7}$$

where I_0 is the magnitude of the current, and $\mathbf{d}$ is the directed distance from source to sink.

[4] Technically, the limit $d \to 0$ refers to the dual limit: $d \to 0$ and $I_0 \to \infty$, such that the product $p = I_0 d$ remains constant and finite.

Dendritic Cable

The current distribution shown in Fig. 2(b) may be written

$$\vec{\nabla} \cdot \mathbf{J}_{\mathrm{S}} = +I_0 \ \delta(x)\delta(y)\delta(z) - i_{\mathrm{m}}(x)\delta(y)\delta(z) \tag{4.8}$$

In both terms, the factors $\delta(y)\delta(z)$ ensure that the source lies on the x-axis. In the first term, the factor $\delta(x)$ puts the sink at $x = 0$. In the second term, the transmembrane current per unit length $i_{\mathrm{m}}(x)$ is given by (2.2).

Inserting (4.8) into (4.3) gives

$$\int \vec{\nabla} \cdot \mathbf{J}_{\mathrm{S}}(\mathbf{r}) \ d^3r = \int_0^\infty \left[I_0 \ \delta(x) - i_{\mathrm{m}}(x) \right] \ dx = 0 \tag{4.9}$$

where the last equality follows from direct integration of (2.2). Thus the monopole contribution vanishes by current conservation, i.e., the total of sources and sinks equals zero.

Inserting (4.8) into (4.5) gives

$$\mathbf{p} = \int \mathbf{r} \left[I_0 \ \delta(x) - i_{\mathrm{m}}(x) \right] \delta(y)\delta(z) \ d^3r \tag{4.10}$$

The three vector components may be evaluated separately. Because of the factor $\mathbf{r} = (x, y, z)$, integration over y and z gives $p_y = 0$ and $p_z = 0$, respectively. Similarly for p_x, integrating over x causes the first term involving $\delta(x)$ to vanish, leaving

$$p_x = -\int_0^\infty x \ i_{\mathrm{m}}(x) \ dx = -I_0 \ \lambda_{\mathrm{m}} \tag{4.11}$$

This result is intuitive: For the ideal dipole (4.6), the dipole moment (4.7) is equal to the current I_0 times the distance d between the source and sink. For the uniform cable with current injected at one end (4.11), the distance d is replaced by λ_{m}, the characteristic length scale for the decay of the current along the dendrite. The minus sign indicates that the direction of extracellular current flow is leftward in Fig. 2(b).

Extracellular Fields of Axons

There are three main arguments that axons make negligible contribution to EEG-MEG. First, the quadrupolar field falls of rapidly with distance, and is likely to be dominated at the scalp by the dipolar fields of dendrites. Second, axons are not arranged systematically in the cortex as are the apical dendrites of pyramidal cells, thus the geometric superposition of axonal fields can not occur to the same degree as it does for dendrites. Third, action potentials have ~ 1 ms duration, and therefore have a dominant frequency near 1000 Hz. The EEG-MEG signal has most of its power below 100 Hz, which is more like the

time scale over which dendritic potentials vary. The extracellular field due to a single neuron is not detectable at the scalp, but the superposition of many synchronously active neurons is detectable. In order for action potential fields to superimpose to measurable levels at the scalp, it would be necessary for the action potentials of multiple neurons to occur with high temporal synchrony. While it does appear that spike synchrony plays a fundamental role in neural processing, the requirements on synchrony are much more demanding for axons than dendrites due to the shorter duration of their potentials. For these reasons, it is expected that EEG-MEG is dominated by dendritic potentials. Up to the size of the integration volume of an EEG or MEG sensor, dipolar sheets created by synchronously active patches of cortex make contributions to the scalp potential in proportion to their size.

For each argument against axon contributions, there is a reasonable counter-argument, First, dipole fields likely dominate the scalp potential, but that does not mean that quadrupole fields are totally negligible. Second, axons run in fiber bundles, and synchronous input to their neurons generates a compound action potential. Third, sensory input typically generates a neural response with abrupt onset and high degree of neural synchrony, at least at the dendritic level. This increases the firing probability in time and can increase spike synchrony. Thus spike synchrony in fiber bundles could potentially superimpose to be measurable at the scalp. Thus, although cortical pyramidal dendrites likely dominate axonal fields in resting EEG, action potentials could conceivably contribute to the scalp potential, particularly in early sensory response. Still, the short duration of spikes puts their power at high frequencies, which are filtered out in many EEG recordings.

5 Human Head Modeling

So far we have assumed an infinite conducting medium, ignoring tissue boundaries and head geometry. The conductivity σ changes abruptly at tissue boundaries, and has major effects on EEG signals recorded at the scalp. Effects on MEG are smaller, but nonzero. The "forward" problem of EEG: Given the brain current sources, compute the electric potential Φ on the scalp are the locations of the measurement and reference electrodes. Since Φ depends linearly on the source currents $\mathbf{J}_{\mathrm{S}}$, linear superposition applies, and it is sufficient to compute the fields due to a single dipole at first.

5.1 Mathematical Considerations

Boundary Conditions

Consider a four-layer head model with conductivity parameters σ_a, where $a = 1, \ldots, 4$, and define the conductivity of air to be $\sigma_5 = 0$. Let Φ_a be the potential in layer a, and let $\hat{\mathbf{n}}$ be the outward-oriented normal to the

boundary surface S. In each layer, σ is constant and the homogenous solution is correct. The solutions to Poisson's equation in each layer are joined together by appropriate boundary conditions.

The first condition boundary condition is that the normal current density $\mathbf{J}_\perp$ be continuous across each boundary:

$$\sigma_a \frac{\partial \Phi_a}{\partial n}\bigg|_S = \sigma_{a+1} \frac{\partial \Phi_{a+1}}{\partial n}\bigg|_S \tag{5.1}$$

where the normal derivative is defined $\partial\Phi/\partial n \equiv \vec{\nabla}\Phi_a \cdot \hat{\mathbf{n}}$. From Maxwell's equation a second boundary condition may be shown: continuity of the parallel component of the electric field. Assuming no sources or sinks on the surface, this is equivalent to continuity of the potential Φ across each boundary:

$$\Phi_a\Big|_S = \Phi_{a+1}\Big|_S \tag{5.2}$$

as may be shown by drawing a rectangular loop with one side in each layer, and integrating the electric field around this loop.

The magnetic field $\mathbf{B}$ obeys similar boundary conditions involving discontinuities in μ (Jackson 1975). These are not relevant to biological tissue, because to high accuracy $\mu = \mu_0$, the magnetic susceptibility of vacuum (Plonsey 1969). Never must we consider discontinuities in μ or boundary conditions on $\mathbf{B}$ in the usual sense. Yet boundary effects do enter at tissue discontinuities. In passing from (3.16) to (3.17) we assumed σ to be constant. Without that assumption we have additional contributions to $\mathbf{B}$ arising from discontinuities in σ. These contributions are identically zero for a spherical head model, but nonzero in general.

Uniqueness of Solution

Poisson's equation for Φ has a unique solution given an appropriate specification of the boundary conditions across the entire surface, including: 1) the potential Φ, or 2) its normal derivative $\partial\Phi/\partial n$, is specified on the boundary (Jackson 1975). These are called Dirichlet and Neumann boundary conditions, respectively. Mixed boundary conditions are also possible, in which Φ and $\partial\Phi/\partial n$ are are specified on non-overlapping parts of the boundary. (Specifying both Φ and $\partial\Phi/\partial n$ over any part of the boundary is an overspecification of the problem, and the existence of a solution is not guaranteed.) This uniqueness property allows us to be creative in how we derive the solution, since finding *any* solution to Poisson's equation which matches the boundary conditions implies that we have found *the* solution.

5.2 Spherical Head Method

The simplest head model that accommodates the layered tissues is comprised an inner sphere (brain) surrounded by 2 (ignoring CSF) or 3 (including CSF)

concentric spheres (see Fig. 1). For a dipole current source at brain location **a** with dipole moment **m**, the potential at the scalp surface location **r** may be written compactly

$$\Phi(\mathbf{r}) = \sum_{n=1}^{\infty} c_n f^{n-1} \mathbf{m} \cdot \left[\hat{\mathbf{r}}\ P_n(\cos\theta) + \hat{\mathbf{t}}\ \frac{P_n^1(\cos\theta)}{n} \right] \tag{5.3}$$

where $f \equiv a/r_4$ is the dipole eccentricity, r_4 is the outer scalp radius, θ is the angle between $\hat{\mathbf{r}}$ and $\hat{a}$, $\hat{\mathbf{r}}$ is the radial unit vector, $\hat{\mathbf{t}}$ is the tangential unit vector, and the c_n are constant coefficients (Salu et al. 1990). Current conservation ensures that the surface integral of the absolute potential Φ induced by a dipolar current source is zero. This is reflected in (5.3) by the absence of a constant term that would be represented by $n = 0$. Thus the potential Φ computed with (5.3) is implicitly referenced to infinity.

In numerical implementations of (5.3), the calculation of the Legendre polynomials $P_n(x)$ is the rate limiting step. Faster implementation is available by noting the convergence properties of the series (Sun 1997).

5.3 Boundary Element Method

The simplest approach for accommodating realistic head geometry keeps the assumption that the head is comprised of four tissue layers: brain, CSF, skull and scalp, and that each layer is described by a single homogeneous and isotropic conductivity σ, but relaxes the assumption of sphericity. Green's theorem may be used to write the solution to Poisson's equation as an integral equation for Φ

$$\Phi(\mathbf{r}_o) = \frac{2\sigma_1}{\sigma_o + \sigma_{o+1}} \Phi_\infty(\mathbf{r}_o) + \frac{1}{2\pi} \sum_{a=1}^{4} \frac{\sigma_a - \sigma_{a+1}}{\sigma_a + \sigma_{a+1}} \int_{\Gamma_a} \Phi(\mathbf{r})\ d\Omega_{\mathbf{r}_o\mathbf{r}} \tag{5.4}$$

where

$$d\Omega_{\mathbf{r}_o\mathbf{r}} \equiv \frac{(\mathbf{r} - \mathbf{r}_o)}{|\mathbf{r} - \mathbf{r}_o|^3} \cdot \hat{\mathbf{n}}\ \mathrm{dS} \tag{5.5}$$

is the solid angle subtended by the surface element dS at $\mathbf{r}$, as viewed from the observation point $\mathbf{r}_o$ (Barnard et al. 1967a; Barnard et al. 1967b; Geselowitz 1967). This equation shows how Φ at each point $\mathbf{r}_o$ in V depends upon the integral of Φ over each tissue boundary surface S, and that the surface contributions are of the same form as a surface dipole layer.

In numerical implementations of (5.4), the basic approach is to discretize the surface with a set of triangular elements, and evaluate the surface integral as a discrete sum. Figure 3 shows surface meshes for this purpose. In setting up the sum, the potential on the surface may be expressed in terms of either the potentials at the corners, or the potentials on the faces. The former is faster computationally because the number of corners is approximately half the number of faces (Barr et al. 1977). It also allows an improvement in which

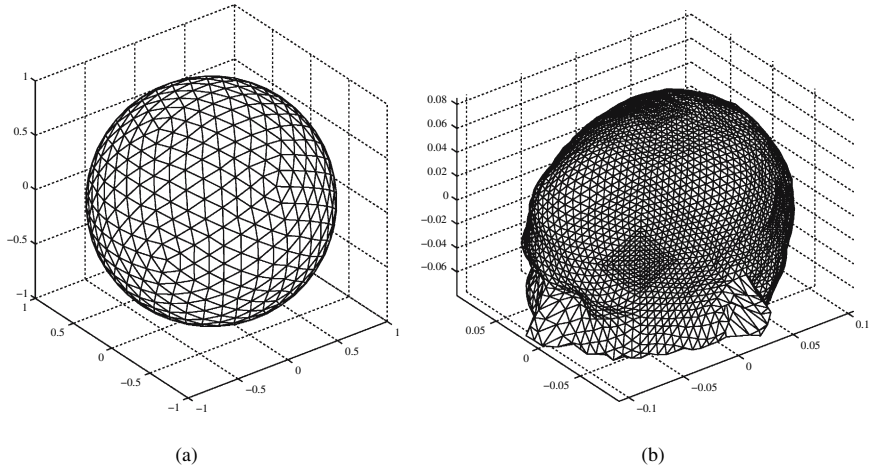

Fig. 3. (**a**) Surface mesh for (**a**) sphere with 1280 faces, (**b**) human scalp with 8192 faces. Meshes are generated on a spherical surface, then fit to the scalp-air boundary of a high-resolution structural MRI

the potential varies linearly over each triangle (Gençer et al. 1999). Evaluating $\mathbf{r}_o$ at each corner leads to a matrix equation for Φ at the corners, which may be solved by inversion. Once Φ is known on S, then (5.4) may be evaluated at any $\mathbf{r}_o$ in V. Scalp potential values at the electrodes may be computed this way, or estimated using spline interpolation (see Sect. 8).

5.4 Conductive Properties of Head Tissues

Aside from inhomogeneities and anisotropies ignored in spherical head models, the conductivity of head tissues are known within some (perhaps large) range of error (Foster and Schwan 1989). The brain conductivity $\sigma_1 \simeq 0.15$ S/m (Stoy et al. 1982). The CSF conductivity $\sigma_2 \simeq 1.79$ S/m (Baumann et al. 1997). The scalp conductivity $\sigma_4 \simeq 0.44$ S/m (Geddes and Baker 1967). The conductivity of the living human skull, however, has been a source of mass confusion. Rush and Blanchard (1966) measured the conductivity ratio between the skull and that of saline in which the skull was immersed, and found conductivity ratios ranging from 50 to 300. Rush and Driscoll (1968) found a ratio near 80, then applied that ratio between the brain and skull, as though the living skull were saturated with brain-like rather than saline-like fluid. Most subsequent studies (e.g., Stok 1987) have used this ratio. Assuming the brain conductivity $\sigma_1 \simeq 0.15$ S/m, for example, $\sigma_1/\sigma_3 \simeq 80$ implies $\sigma_3 \simeq 0.002$ S/m.

Since then evidence has accumulated that this early reasoning may greatly underestimate σ_3. Even within the context of the Rush and Driscoll (1968) study, assuming the saline conductivity $\sigma \simeq 1.3$ S/m implies $\sigma_3 \simeq 0.017$ S/m. Kosterick et al. 1984 reported $\sigma_3 \simeq 0.012$ S/m. Averaging the values reported in Law et al. (1993) suggests $\sigma_3 \simeq 0.018$ S/m. Oostendorp et al.

(2000) reported $\sigma_3 \simeq 0.015$ S/m. This series of literature seems to implies consistently that $\sigma_3 \simeq 0.015$ S/m and $\sigma_1/\sigma_3 \simeq 10$. This ratio is lower than the range 20–80 suggested by Nunez and Srinivasan (2005), due partly to a lower estimate of brain conductivity. With this skull conductivity, assuming the brain conductivity $\sigma_1 \simeq 0.33$ S/m (Stok 1987), for example, gives the ratio $\sigma_1/\sigma_3 \simeq 22$. Early models assumed the brain and scalp conductivity were equal (Rush and Driscoll 1968). If this skull conductivity is compared to the scalp rather than the brain, $\sigma_4/\sigma_3 \simeq 29$.

As discussed in Nunez and Srinivasan (2006), however, the effective conductivity of a single layered skull used in a volume conductor model may be substantially lower than its actual conductivity due to several shunting tissues not included in such models, e.g., extra CSF, the middle skull layer, and the anisotropic white matter. For example, consider a three-layered skull in which the inner skull layer conductivity is substantially higher than the inner and outer skull layers (as verified experimentally). Imagine a limiting case where the resistivity of the inner layer goes to zero so that no current enters the outer skull layer or scalp (zero scalp potential everywhere). The effective brain-to-skull conductivity ratio is infinite in this limiting case, even though the measured value based on a composite skull could easily be less than 20. This argument implies that effective brain-to-skull conductivity ratios cannot be accurately estimated from impedance measurements of composite skull tissue alone.

6 Data Acquisition

6.1 Electrode and Amplifier Systems

In EEG recordings, electric potential is measured on the scalp surface, and used to make inferences about brain activity. Although potentials relative to infinity are often considered in theoretical derivations, in practice only potential differences can be measured. Thus EEG measurements always involve the potential difference between two sites. This is accomplished using differential amplifiers, which include the measure electrodes, a reference electrode, and an "isolated common" electrode that takes the place of true ground.

Huhta and Webster (1973) presented an essentially complete analysis of electrocardiographic (ECG) recordings using differential amplifiers, including signal loss and 60 Hz noise. Several of their assumptions are either outdated or not applicable to EEG. First, they assumed that the subject was resistively coupled to earth ground. This simplification reduces the number of variables in the calculations, but is unsafe because it increases the risk of electric shock. It also allows more 60 Hz noise to enter the measurements because ambient electric potential fields in the recording environment exist relative to earth ground. Second, they assumed the grounding electrode was connected to the subjects foot, at maximal distance from the recording and reference electrodes

which were located on the torso for cardiac recording. The thinking was that the foot would be electrically quiet, which may be true, but this increases 60 Hz noise because the entire body acts as an antenna.

Modern EEG systems are designed differently (Ferree et al. 2001). First, safety regulations require that the subject be isolated from ground so that contact with an electric source would not result a path to earth ground. This is accomplished by using an "isolated common" electrode that is electrically isolated from the ground of the power supply. In this configuration, the subject is only capacitively coupled to true ground, largely eliminating the risk of electric shock, and reducing 60 Hz noise. The measurement is then made as follows. The potential of both measurement and reference leads are taken relative to the common electrode, then their difference is amplified. Second, both the reference and common electrodes are located on the head in order to minimize 60 Hz common-mode noise sources, as well as physiological noise from cardiac sources.

6.2 Temporal Sampling

The validity of the quasi-static approximation to Maxwell's equations in biological materials is equivalent to saying that the electric and magnetic fields propagate from the brain to the scalp instantaneously. In this sense, the temporal resolution of EEG (and MEG) is unlimited. Because most of the power in EEG time series falls below 100 Hz, typical sampling rates are 250 Hz, 500 Hz, and 1 kHz. Higher sampling rates are used to measure the brain-stem auditory evoked potential, and to adequately represent artifacts when EEG is recorded simultaneously with fMRI, but usually lower sampling rates are preferred because they result in smaller file sizes and faster analysis.

In digital signal processing, the Nyquist theorem states that power at frequency f in a signal must be sampled with interval $\Delta t \leq 1/(2f)$. For fixed Δt, this means that only frequencies $f \leq 1/(2\Delta t)$ are accurately represented; this is called the Nyquist frequency. Power at frequencies $f > 1/(2\Delta t)$ are aliased, i.e., represented inaccurately as power at lower frequencies. To avoid this, EEG and other amplifiers sample in two stages. For a given choice of sampling rate Δt, analog filters are applied to remove signal power at frequencies $f > 1/(2\Delta t)$, then the signal is sampled discretely. In this way, EEG amplifiers have a wide range of sampling rates that may be selected without aliasing.

6.3 Spatial Sampling

In clinical EEG, speed, convenience, and culture typically dictate that only 19 electrodes be used, with inter-electrode spacing around 30 degrees. This configuration reveals large-scale brain activity reasonably well, and taking the potential difference between neighboring electrode pairs can isolate focal activity between those electrodes provided other conditions are met. Generally speaking, however, this low density misses much of the spatial information in the scalp potential. In research EEG, electrode arrays typically have 32, 64,

128, or 256 recording channels. The more electrodes, the more information, but there is a limit to the improvement.

The skull tends to smooth the scalp potential, compared to the brain surface or inner skull surface potential. Srinivasan et al. (1998) used spherical head models to quantify this effect. They generated random, many-dipole configurations in the cortex, and computed the scalp surface potentials. They sampled the scalp potential discretely using 19-, 32-, 64, and 128-channel arrays, and quantified the map differences for each array. They concluded that 128 electrodes are necessary to capture most of the spatial information available in the scalp potential, and that fewer than 64 channels can result in significant sampling errors. As in the time domain, if the scalp topography is sampled too sparsely, it suffers from aliasing artifacts. In the spatial domain, however, aliasing due to under-sampling can not be corrected by pre-filtering, as is done in the time domain.

7 Lead Field Theory

This section describes a useful way of thinking about the spatial resolution of scalp EEG. Previous sections described how each dipole (specified by position and orientation) gives a unique scalp potential. In this way of thinking, the potential for a single dipole is normally computed at all electrodes. Alternatively, the same problem may be arranged so that the potential difference across a single electrode pair is computed for each dipole position and orientations. This yields the *lead field vector* $\mathbf{L}$ for each electrode pair, which may be computed from the electric field that would exist in the head if current were injected into those same electrodes. This seems less intuitive but, insofar as scalp measurements integrate over the activity of large cortical areas (10–100 cm^2), this leads to a metric for the field of view of each electrode pair. The tabulation of the potential at every electrode, for each of a large but finite number of dipole locations and orientations in the brain, is called the *lead field matrix*. This quantity summarizes all the information about the head model, and is the starting point for inverse solutions.

7.1 Heuristic Definition

Imagine that a single dipole is placed at a point $\mathbf{r}_p$ inside a volume conductor, and oriented along the positive x-axis. Make no assumptions about the shape, homogeneity or isotropy of the volume conductor. Let $\Delta\Phi$ be the potential difference measured across two surface electrodes, and p_x be the dipole strength. Because Poisson's equation is linear in the sources, $\Delta\Phi$ must depend linearly upon the strength of the dipole, and this may be written algebraically as

$$\Delta\Phi = L_x p_x \tag{6.1}$$

where L_x is a proportionality constant. At the point $\mathbf{r}_p$, similar relations hold for the other two dipole orientations. If there were three perpendicular dipoles,

one along each of three Cartesian axes, then $\Delta\Phi$ would be the linear sum of each contribution.

$$\Delta\Phi = L_x p_x + L_y p_y + L_z p_z = \mathbf{L} \cdot \mathbf{p} \tag{6.2}$$

where the last equality derives simply from the definition of vector dot product. The quantity $\mathbf{L}$ is called the *lead field vector*. Strictly speaking we have not shown that $\mathbf{L}$ behaves as a vector under coordinate transformations, but it must if its contraction with the vector $\mathbf{p}$ is to yield a scalar $\Delta\Phi$.

7.2 Reciprocity Theorem

The reciprocity theorem (Helmholtz, 1853) gives an explicit expression for $\mathbf{L}$. The mathematical techniques used in deriving it are similar to those used in boundary element modeling. Consider a conducting volume V bounded by a surface S. Make no assumptions about the shape or homogeneity of the volume conductor.[5] Figure 4 shows two source and measurement configurations, denoted t_1 and t_2.

In configuration t_1, the source is a dipole located in the volume and the measurement is made by surface electrodes at positions $\mathbf{r}_\mathrm{A}$ and $\mathbf{r}_\mathrm{B}$. In configuration t_2, the source is introduced "reciprocally" by injecting current through the surface electrodes, and the potential difference is considered across the dipole. Now use Green's theorem to relate the potential Φ in one configuration to the current density $\mathbf{J}$ in the other. Consider the quantities

$$\vec{\nabla} \cdot [\Phi_1 \mathbf{J}_2] = \vec{\nabla}\Phi_1 \cdot \mathbf{J}_2 + \Phi_1 \vec{\nabla} \cdot \mathbf{J}_2$$
$$\vec{\nabla} \cdot [\Phi_2 \mathbf{J}_1] = \vec{\nabla}\Phi_2 \cdot \mathbf{J}_1 + \Phi_2 \vec{\nabla} \cdot \mathbf{J}_1$$

where $\mathbf{J}_i = -\sigma_i \vec{\nabla}\Phi_i$ for $i = 1, 2$. Subtracting these equations and assuming that $\sigma_1 = \sigma_2 = \sigma$, the first terms on the RHS of each equation cancel. By assumption $\vec{\nabla} \cdot \mathbf{J}_2 = 0$ in V and $\mathbf{J}_1 \cdot \hat{\mathbf{n}} = 0$ on S. Integrating over the volume V and using the divergence theorem to write the LHS as a surface integral over S leads to

$$\int_S \Phi_1 \ \mathbf{J}_2 \cdot \hat{\mathbf{n}} \ dS = -\int_V \Phi_2 \ \vec{\nabla} \cdot \mathbf{J}_1 \ dV \tag{6.3}$$

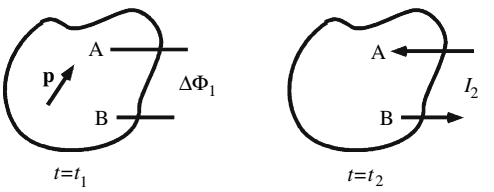

Fig. 4. Reciprocal source and measurement configurations for EEG reciprocity theorem

[5] The derivations presented here assume isotropy for simplicity.

In configuration t_1, let the current source and sink be located at $\mathbf{r}_\pm = \mathbf{r}_1 \mp \mathbf{d}/2$ and let the dipole strength be $p = I_1 d$, where d is the dipole separation. We have

$$\vec{\nabla} \cdot \mathbf{J}_1 = I_1 \left[\delta^{(3)}(\mathbf{r} - \mathbf{r}_+) - \delta^{(3)}(\mathbf{r} - \mathbf{r}_-) \right] \tag{6.4}$$

where the sign convention is such that $\mathbf{J}_1 = -\sigma_1 \vec{\nabla} \Phi_1$. In the notation of (3.12), $\vec{\nabla} \cdot \mathbf{J}_1 = \vec{\nabla} \cdot \mathbf{J}_\mathrm{E} = -\vec{\nabla} \cdot \mathbf{J}_\mathrm{S}$.

In configuration t_2, let $\mathbf{r}_\mathrm{A}$ be the location of the source electrode, which injects current into the head by establishing a positive potential at that point, and let $\mathbf{r}_\mathrm{B}$ be the location of the sink electrode, which extracts current from the head by establishing a negative potential at that point. The normal component of the current density on the surface may then be written formally

$$\mathbf{J}_2 \cdot \hat{\mathbf{n}} = I_2 \left[\delta^{(2)}(\mathbf{r} - \mathbf{r}_\mathrm{B}) - \delta^{(2)}(\mathbf{r} - \mathbf{r}_\mathrm{A}) \right] \tag{6.5}$$

Inserting (6.4) and (6.5) into (6.3) and performing the integrals trivially over the delta functions gives

$$I_2 \left[\Phi_1(\mathbf{r}_\mathrm{A}) - \Phi_1(\mathbf{r}_\mathrm{B}) \right] = -I_1 \left[\Phi_2(\mathbf{r}_+) - \Phi_2(\mathbf{r}_-) \right] \tag{6.6}$$

Expanding the difference $\Phi_2(\mathbf{r}_\pm)$ in powers of d and taking the usual dipole limit as $d \to 0$ gives

$$\Phi_1(\mathbf{r}_\mathrm{A}) - \Phi_1(\mathbf{r}_\mathrm{B}) = \mathbf{p} \cdot \mathbf{L} \tag{6.7}$$

where the lead field vector is defined

$$\mathbf{L} = -\frac{\vec{\nabla} \Phi_2(\mathbf{r}_1)}{I_2} = \frac{1}{\sigma(\mathbf{r}_1)} \frac{\mathbf{J}_2(\mathbf{r}_1)}{I_2} \tag{6.8}$$

Thus the lead field vector $\mathbf{L}$ for a particular electrode pair (A,B) is proportional to the current density $\mathbf{J}_2$ which would be created in V at the dipole position $\mathbf{r}_1$ if unit current I_2 were injected through the electrode pair. The proportionality constant is the reciprocal of the local conductivity σ at the dipole location $\mathbf{r}_1$.

The lead field $\mathbf{L}$ has the content of the usual forward problem, but is interpreted somewhat differently. It is computed as a function of the dipole position for fixed electrode positions. That is opposite the normal formulation of the forward solution, in which the potential at any point is computed for fixed dipole location. In this way the lead field gives a measure of the sensitivity of a particular electrode pair to dipoles are arbitrary locations in the volume. This may be used to reduce the computational demand of the forward problem for a fixed electrode array.

7.3 Spatial Sensitivity of EEG

The lead field vector $\mathbf{L}$ is the proportionality constant between $\mathbf{p}$ and $\Delta\Phi$, and is a measure of the sensitivity of an electrode pair to dipoles at various

locations. Since the orientation dependence implemented by the dot product is rather trivial, the magnitude of the lead field vector $L \equiv |\mathbf{L}|$ may be defined as the sensitivity of an electrode pair (Rush and Driscoll 1968). The amount of tissue probed by a particular pair may be quantified through the concept of half-sensitivity volume (Malmivuo and Plonsey 1995; Malmivuo et al. 1997).

The half-sensitivity volume (HSV) is defined as follows. For a given electrode pair, we compute the scalar sensitivity $L(\mathbf{r})$ for many ($\sim 10^4$) points $\mathbf{r}$ inside the brain volume, and determine the maximum sensitivity $L_{\max}$ for this pair. We then identify all points in the brain volume whose sensitivity is at least $L_{\max}/2$. The HSV is the volume filled by these points. The threshold of $1/2$ is certainly arbitrary, but does give some indication of the volume in which the largest sensitivities occur. We further define the depth D of the sensitivity distribution as the maximum depth of all points included in the HSV. Using a four-sphere model of the human head, the outer radii of the four tissue layers are 8.0 cm (brain), 8.2 cm (CSF), 8.7 cm (skull) and 9.2 cm (scalp).

Figure 5 shows $\mathbf{L}$ in a two-dimensional plane including the electrodes (A,B) and the origin. The vector nature of $\mathbf{L}$ is retained to illustrate its dependence

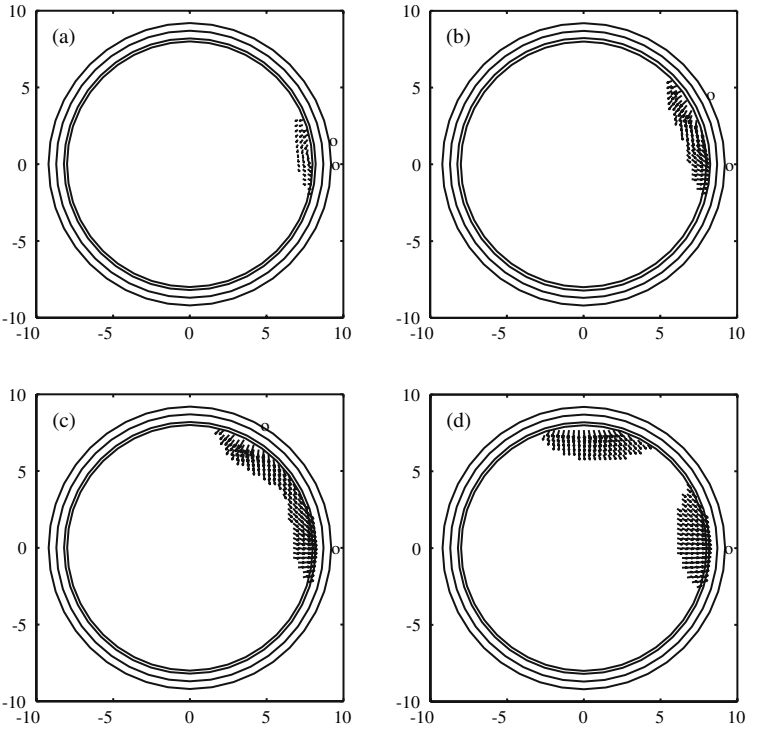

Fig. 5. The EEG lead field vector $\vec{L}(\vec{r})$ shown only within the HSV, for a four-sphere head model with $\sigma_3/\sigma_4 = 1/24$. The electrode separation angles θ are: (**a**) 10, (**b**) 30, (**c**) 60 and (**d**) 90 degrees. Axes are in cm

on orientation, but only its magnitude $L = |\mathbf{L}|$ is used to define the sensitivity and the HSV. In such a simple head model, the HSV is seen to be a single contiguous volume for nearby electrode pairs, which bifurcates near 60 degrees into two separate volumes for more distant pairs. Like the potential difference $\Phi_A - \Phi_B$, the lead field $\mathbf{L}$ changes only by a minus sign under interchange of A and B; the geometric pattern of sensitivity is unaffected.

The vector direction of $\mathbf{L}$ shows how the direction sensitivity of EEG bipolar recordings changes as a function of angle θ between the electrodes. Between nearby electrodes the sensitivity is primarily tangential to the sphere, while under each electrode the sensitivity is more radial. This observation refines the intuition that nearby electrodes are primarily sensitive to tangential dipoles between them. In fact, the greatest sensitivity lies not between the electrodes, but under each electrode, and has a significant radial component. For distant electrodes, the sensitivity is localized under each electrode separately. It is primarily radial, yet on the periphery of each lobe of the HSV there is some tangential component. This observation refines the intuition that distant electrodes are primarily sensitive to radial dipoles. In summary, both nearby and distant electrodes are sensitive to both radial and tangential dipoles. In both cases, the location of maximum sensitivity is directly under the electrodes, where the lead field $\mathbf{L}$ is oriented nearly radially. Thus EEG is predominantly but not exclusively sensitive to radial dipoles. This effect is enhanced by the fact that cortical gyri are populated with radial dipoles and are located closer to the detectors than are sulci.

Figures 6 and 7 show summarizations of the HSV results as a function of the angle θ between electrodes in the visualization plane. Intuitively, the smaller the HSV, the more refined an estimate of dipole position can be made

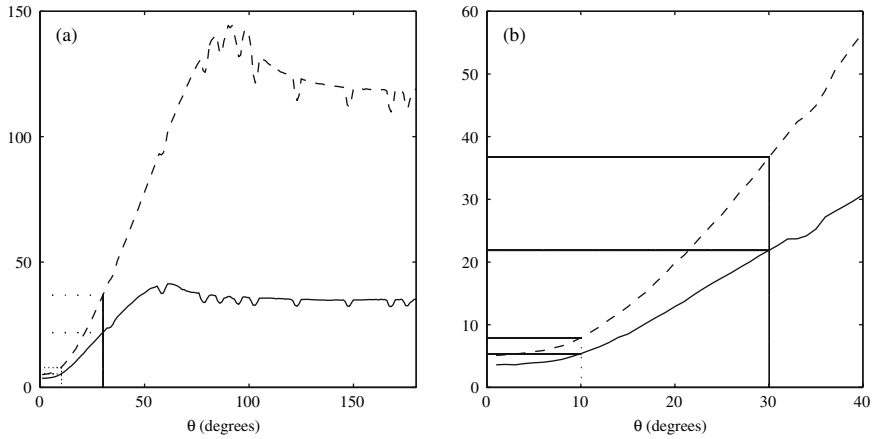

Fig. 6. Half-sensitivity volume (HSV) as a function of electrode separation angle θ, for $\sigma_3/\sigma_4 = 1/24$ (solid) and $\sigma_3/\sigma_4 = 1/80$ (dashed). Figure (**a**) is expanded in (**b**) for small θ

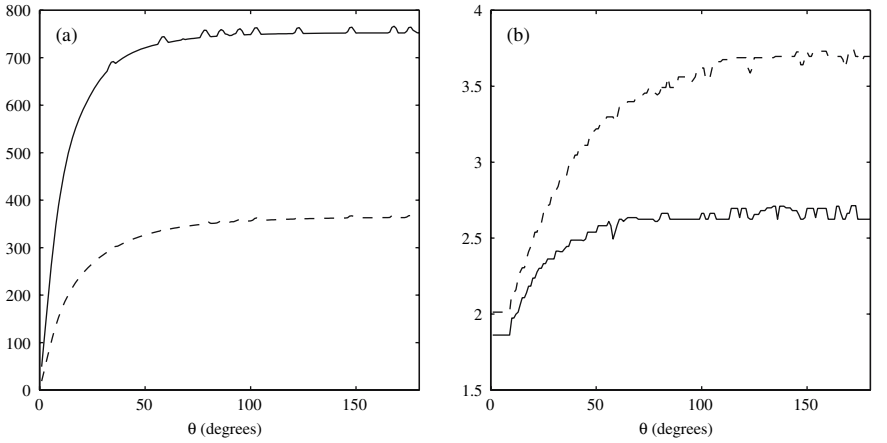

Fig. 7. (**a**) Maximum sensitivity $L_{\max}$ (Ω/m), and (**b**) depth of HSV (cm) as a function of electrode separation angle θ. Line types are the same as in Fig 2. Depth is defined relative to the scalp surface, which is separated from the brain surface by 1.2 cm

from a single electrode pair. Figure 6 shows the HSV as a function of angle. It increases rapidly as a function of angle until the bifurcation occurs, then decreases slightly. For very small θ, the HSV reaches an effective minimum. This limiting behavior can be understood in two complementary ways: In terms of the lead field vector computed via scalp current injection, for nearby electrodes most of the current is shunted through the scalp and little passes into the head volume. In terms of dipolar source currents, the brain potential is blurred by the skull such that nearby scalp electrodes sense nearly identical potentials. For conventional 19-electrode systems, for which nearby pairs are separated by 30 degrees, we find an optimal spatial resolution (minimum HSV) of 22–37 cm^3. For modern 129-electrode systems, for which nearby pairs are separated by more like 10 degrees, we find an optimal spatial resolution of 6–8 cm^3.

Two other sensitivity measures are maximum sensitivity and depth of sensitivity, shown in Fig.7. The maximum sensitivity (Fig. 7a) rises abruptly from near zero at small θ and approaches an asymptote. The maximum sensitivity is found at 180 degrees, and is 350–750 Ω/m depending on skull conductivity. The depth of sensitivity (Fig. 7b) varies similarly as a function of θ, with the exception of an abrupt minimum below 10 degrees. Like the small bumps visible in Figs. 6 and 7, the exact nature of this minimum appears to be artifactual, depending upon how the electrodes sit in relation to the Cartesian grid used to compute these quantities. The maximum depth is found at 180 degrees, and is 2.6–3.7 cm for this range of choices of skull conductivity.

Because of the folds of the cortical sheet, it is difficult to estimate the number of neurons detected by a particular electrode pair, without basing the analysis on a subject-specific structural MRI. In general, for nearby electrodes the HSV is confined almost entirely to the cortical sheet. Assuming the sheet is 0.25 cm thick and densely folded, these volume estimates above can be translated into effective cortical surface area estimates. Dividing the minimum HSV by the cortical thickness gives 88–148 cm^2 at 30 degrees, and 24–32 cm^2 at 10 degrees. Each 1 cm^2 of cortex is populated by approximately 10^7 pyramidal neurons (see Sect.2). This implies that on the order of 10^9 neurons reside inside the HSV at 30 degree electrode separation, and on the order of 10^8 at 10 degree electrode separation. These estimates are inflated, however, because some of the HSV includes noncortical tissue, and because cortical geometry excludes many neurons from detection when the local cortical surface is not parallel to the lead field. Nevertheless, these HSV measure provide a useful and intuitive metric of the spatial resolution of scalp EEG.

8 Topographic Analysis

As seen in Sects. 6 and 7, the reference electrode is an unavoidable fact in EEG recordings. Apart from attempts at optimal placement, several data processing methods exist for reducing or eliminating its influence. These include the average reference, the surface Laplacian, and inverse techniques which solve for brain dipole sources. The first two are specific to EEG, and avoid the ill-posed inverse problem. They make no explicit assumptions about the distribution of brain dipole sources, do not require head volume conductor models, and are computationally efficient. The average referenced scalp potential approximates the scalp potential referenced to infinity, and the surface Laplacian estimates the dura surface potential making the reasonable assumption of low skull conductivity. This section develops these ideas as simple and effective ways of handling the reference electrode issue in scalp EEG. Inverse methods based upon volume conductor models are discussed in the chapter by R. Leahy, and are applicable to both EEG and MEG.

8.1 EEG Reference Effects

At each time point, the definition of the electric potential by $\mathbf{E} = -\vec{\nabla}\Phi$ implies that Φ is ambiguous up to a constant. Physicists usually choose to reference Φ to infinity, so that the potential at infinity is zero by definition. This simplifies derivations and allows the potential at finite distances to be treated as a function of only one spatial variable. EEG recording systems with N amplifier channels record N potential differences from a common reference. If the reference electrode is located at the vertex, for example, then the potential differences measured at nearby electrodes will typically be smaller. Topographic maps of the raw potential, or derived quantities such as the Fourier power spectrum, will tend toward zero as the distance to the vertex is reduced,

The simplest attempt at eliminating the effect of the reference is to place it advantageously, i.e., away from active brain sources. Common choices include the earlobes, the nose, and the mastoids. The earlobes and nose are interesting, in light of the fact that electric potential tends to vary rapidly near pointed objects (Jackson 1975). The mastoids ensure secure attachment, which is most crucial for the reference electrode, but are clearly sensitive to brain activity in inferior posterior brain areas. Each of these are legitimate choices, although perhaps not effective in reaching their goal. Another approach, which should be avoided, is the linked-ears or linked-mastoids reference, in which electrodes are placed on both ears or mastoids, then physically linked before connecting to the reference input of the amplifier. EEG amplifiers are designed with high input impedances, specifically so they will not permit significant current flow across the scalp-electrode boundary. This reference choice violates that basic design principle, and leads to major problems. First, the linking introduces an highly conducting pathway between the two ears. This forces the ears to have similar potentials, which would not otherwise be the case for any singular choice of reference. In the limit of low scalp-electrode impedances, which is always the goal of electrode attachment, the potentials at the two reference sites are identical. Second, the impedances of the two reference electrodes are unlikely to be identical, so this choice is unlikely to be symmetrical as intended. Third, by violating the assumption of zero normal current flow though the scalp, the data are not suitable for analysis by the many commercial and open-source software packages. Fourth, because the basic physics of the problem has been altered, it is not possible simply to re-reference the data to other single electrodes.

8.2 Average Reference

The *average reference* is a simple way of estimating the potential at the reference electrode relative to infinity (Nunez 1981). At each time point, this quantity is used to compute the potentials at each measurement electrode relative to infinity (Bertrand et al. 1985). Because the genuine average reference can not be determined precisely, the operational average reference (based on limited sampling) has received valid criticism (Tomberg et al. 1990; Desmedt and Tomberg 1990) in favor of explicit references (Gencer et al. 1996; Geselowitz 1998), the surface Laplacian (Hjorth 1975; Nunez 1981), or more complicated methods (Lehmann et al. 1986; Yao 2001; Orekhova et al. 2002). Still it remains a useful technique for data analysis and visualization.

Biased Estimate

Let $\Phi(\mathbf{r})$ denote the scalp potential at point $\mathbf{r}$ measured relative to infinity, i.e., the *absolute* scalp potential. Let V_i denote the scalp potentials measured at electrodes $i = 1, ..., N$. The last electrode $i = N$ is the reference electrode for which $V_N \equiv 0$. For a perfect EEG amplifier system, we have $V_i = \Phi_i - \Phi_{\text{ref}}$,

where $\Phi_i = \Phi(\mathbf{r}_i)$, and $\Phi_N = \Phi_{\text{ref}}$ is the absolute potential at the reference electrode. We seek Φ_i but measure V_i; the difference amounts to estimating Φ_{ref}.

Let $\bar{V}$ denote the average of the potentials measured at N scalp electrodes:

$$\bar{V} \equiv \frac{1}{N} \sum_{i=1}^{N} V_i \tag{10.1}$$

Let U_i denote the average referenced potentials, i.e., re-referenced according to the definition $U_i \equiv V_i - \bar{V}$. The U_i have the property

$$\frac{1}{N} \sum_{i=1}^{N} U_i = \frac{1}{N} \sum_{i=1}^{N} \left(V_i - \bar{V}\right) = \left(\bar{V} - \bar{V}\right) = 0 \tag{10.2}$$

Because the sum over the U_i vanishes like the surface integral of Φ, the U_i are taken to estimate the Φ_i, with $\Phi_{\text{ref}} \equiv \Phi_N \simeq U_N = -\bar{V}$. This estimate is biased by not including contributions from the inferior head surface: the polar average reference effect (Junghofer et al. 1999).

Unbiased Estimate

Spherical splines were developed for topographic mapping of the scalp surface potential and the surface Laplacian (Perrin et al. 1989; Perrin et al. 1990), but their mathematical form carries implicitly an estimate of the average surface potential. Let $V(\mathbf{r})$ be the potential at an arbitrary point r on the surface of a sphere of radius r, and let $\mathbf{r}_i$ be the location of one the i^{th} measurement electrode. Spherical splines represent the potential at r on the surface of the sphere by

$$V(\mathbf{r}) = c_0 + \sum_{j=1}^{N} c_i \; g_m \left(\cos(\hat{\mathbf{r}} \cdot \hat{\mathbf{r}}_j)\right) \tag{10.3}$$

where the function $g_m(x)$ is given by

$$g_m(x) = \frac{1}{4\pi} \sum_{n=1}^{\infty} \frac{2n+1}{(n(n+1))^m} P_n(x) \tag{10.4}$$

The functions $P_n(x)$ are the Legendre polynomials of order n, which form a complete set of basis functions on a spherical surface.[6]

[6] The use of ordinary Legendre polynomials does not imply that the surface potential must have azimuthal symmetry. The variable x in $P_n(x)$ represents the angle between electrode position $\mathbf{r}_i$ and the interpolation point $\mathbf{r}$, so the claim is that (10.3) is capable of fitting the net scalp potential without inherent symmetry.

Recently we elaborated the idea put forth in Junghofer et al. (1999) that the spherical splines permit a better estimate of the average surface potential (Ferree 2006). Integrating (10.3) over the entire spherical scalp surface, and using that the integral of $P_n(x)$ on $-1 \leq x \leq +1$ vanishes for $n \neq 0$ (Arfken 1995), leads to

$$c_0 = \frac{1}{4\pi r_4^2} \int V(\mathbf{r})\ dS \tag{10.5}$$

where r_4 is the outer scalp radius. Thus the coefficient c_0 is equal to the average of the *interpolated* potential over the sphere surface.

Current conservation implies that, for dipolar current sources in an arbitrary volume conductor, the surface integral of the absolute potential Φ vanishes (Bertrand et al. 1985). Substituting $V(\mathbf{r}) = \Phi(\mathbf{r}) - \Phi_{\text{ref}}$ leads to

$$c_0 = \frac{1}{4\pi r_4^2} \int (\Phi(\mathbf{r}) - \Phi_{\text{ref}})\ dS \simeq -\Phi_{\text{ref}} \tag{10.6}$$

Based upon (10.6), we expect c_0 to provide a *reasonable* estimate of Φ_{ref}, which can be used to compute the absolute potentials using $\Phi_i = V_i + \Phi_{\text{ref}} \simeq V_i - c_0$. This favorable situation is limited by the fact that the spline fit is severely under-constrained on the inferior head surface, and is unlikely to be numerically accurate there. It is conceivable that the estimate $\Phi_{\text{ref}} \simeq -c_0$ is *worse* than the usual estimate $\Phi_{\text{ref}} \simeq -\bar{V}$, but further investigation proved otherwise. A more convincing theoretical argument and numerical simulations showing that spherical splines generally provide a *better* estimate of Φ_{ref} are given in (Ferree 2006).

8.3 Surface Laplacian

Complementary to the scalp potential is the scalp surface Laplacian, the second spatial derivative of the potential. Practically speaking, the surface Laplacian solves the problem of the reference electrode because the second spatial derivative discards any overall constant (corresponding to the potential at the reference electrode relative to infinity). The calculation of the surface Laplacian is made separately at each time point. Physically, it is most directly related to the local current density flowing radially through the skull into the scalp. Because current flow through the skull is mostly radial, the scalp surface Laplacian remarkably provides an estimate of the dura potential (Nunez 1987). Numerical simulations using real data have shown that the surface Laplacian has 80–95% agreement with other dura imaging algorithms (Nunez and Srinivasan 2006). This connection between the scalp surface Laplacian and dura potential is derived next.

The following derivations make three main assumptions: 1) the current flow through the skull is nearly radial, 2) the potential drops across the scalp and CSF are small, at least compared to that across the skull, and 3) the

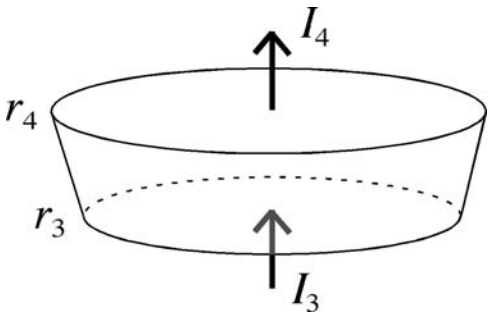

Fig. 8. A patch of scalp for consideration of the surface Laplacian in Problem 1. The parameter r_3 represents the outer skull surface, and r_4 the outer scalp surface. Alternatively, by replacing $3 \rightarrow 2$ and $4 \rightarrow 3$, the same figure may be used to represent a patch of skull in Problem 2

potential on the brain surface is much larger in amplitude than that on the scalp surface, by close proximity to the dipolar sources. Referring to Fig. 8, we have

$$I_3 = \int_S \mathbf{J}_4 \cdot \hat{t}\, d\Gamma \tag{10.7}$$

where Γ is the surface on the sides of the scalp patch, and $\hat{t}$ is a unit vector normal to Γ and therefore tangential to the scalp-air boundary. Assume that $\Phi_4(r, \theta, \phi)$ depends negligibly on r (on the grounds that the scalp is thin and σ_4 is high, at least compared to σ_3), so that $\Phi_4(r, \theta, \phi) \simeq V(\theta, \phi)$ leads to

$$I_3 \simeq -\sigma_4(r_4 - r_3)A_4\nabla_s^2 V \tag{10.8}$$

where A_4 is the cross-sectional area of the scalp patch. The boundary condition on $J_\perp$ on each side of the skull implies that the current flow through the skull is primarily radial, thus $I_2 = I_3$. Given that, the potential within the skull patch must vary radially according to the function

$$\Phi_3(r) = \frac{a}{r} + b \tag{10.9}$$

Considering how the cross-sectional area of the patch $A(r)$ varies as a function of r, and making use of the boundary condition on $J_\perp$ at the skull-scalp boundary r_3, shows that the potential difference across the skull is given approximately by

$$\Phi_3(r_2) - \Phi_3(r_3) = (r_3 - r_2)\frac{I_3}{\sigma_3}\frac{r_3}{r_2}\frac{1}{A_3} \tag{10.10}$$

Making use of the boundary condition on Φ leads to

$$\Phi_2(r_2) - \Phi_4(r_3) = -\frac{\sigma_4}{\sigma_3}\frac{r_4^2}{r_2 r_3}(r_4 - r_3)(r_3 - r_2)\nabla_s^2 V \tag{10.11}$$

which states that the potential difference across the skull is approximately proportional to the surface Laplacian. Finally, assuming that: 1) the potential drop across the CSF is small compared to that across the skull due to the low skull conductivity and high CSF conductivity, and the fact that the CSF layer is thinner than the skull, and 2) that the potential on the dura surface $\Phi_d = \Phi_2(r_1) = \Phi_1(r_1)$ is large compared to the potential on the scalp surface $\Phi_4(r_4) = V$, leads to

$$\Phi_d \simeq -\frac{\sigma_4}{\sigma_3}\frac{r_4^2}{r_2 r_3}(r_4 - r_3)(r_3 - r_2)\nabla_s^2 V \tag{10.12}$$

Thus the scalp surface Laplacian is proportional to the dura potential. Because the scalp surface Laplacian acts as a spatial high-pass filter (Nunez and Srinivasan 2006), possibly missing some valid information in the data, it is best used in conjunction with the average-referenced potential to study brain dynamics on the scalp.

8.4 Bipolar Pairs

Another way of eliminating the reference electrode effect is to based studies on bipolar pairs, as is common in clinical practice. Figs. 5(a) and (b) show that the potential difference between nearby electrode pairs have spatial sensitivity that is restricted to their local. The potential difference between all such pairs, or perhaps only nearest-neighbor pairs, may be computed easily and completely eliminates the dependence on the original reference electrode. Whereas the previous two approaches, the average reference and surface Laplacian, eliminated the dependence on the reference electrode, this approach makes explicit use of the reference electrode by effectively moving it around to form local bipolar pairs. Time-domain averages (i.e., event-related potentials) or power spectra computed from these time series are representative of the associated HSV, although the results are difficult to show graphically because each temporal or spectral measure is associated with one electrode rather than two. Time series collected from two bipolar pairs, which are themselves widely separated (e.g., a nearby pair in occipital cortex and a nearby pair in frontal cortex) may also be used for coherence analysis (Nunez 1995).

9 Summary

This goal of this chapter is to provide a rigorous introduction to scalp EEG for research in functional connectivity. We started at the microscopic level and discussed the cellular basis of current sources that generate extracellular fields, and developed the steps in electromagnetic theory that describe macroscopic fields in biological systems. We discussed the solutions to the EEG forward

problem in spherical and realistic head models. We also discussed EEG measurement technology, to make clear the reasons why the reference electrode issue arises so frequently in EEG experiments. We developed the concept of the lead field vector **L** to help visualize the spatial sensitivity patterns of scalp electrode measurements. These arguments lead to the conclusion that the reference electrode acts as a measurement electrode, and this fact must be addressed before drawing conclusions about the activity under any single electrode.

Studies of functional connectivity involve temporal measures of correlation, e.g., coherence and Granger causality, applied to two or more electrodes. Implicitly it is assumed that the time series collected at each electrode detects brain activity near that electrode. Our arguments using lead field theory show that each electrode is sensitive to large tissue volumes, containing perhaps 10^8–10^9 cortical neurons. Thus EEG measures of functional connectivity apply only to very large spatial scales, although somewhat smaller scale connectivity may be estimated with high resolution EEG methods like the surface Laplacian.

The reference electrode continues to confound many EEG studies. This chapter presented three practical ways of dealing with the reference electrode issue: adopting the average reference, the scalp surface Laplacian, or bipolar pairs. These data transformations and related concepts are essential to the estimation of temporal and spectral measures that may be used to make inferences about functional connectivity. Other facets of these topics are described elsewhere (e.g., Nunez and Srinivasan 2006).

Acknowledgements

This work was supported in part by NIH grants R43-MH-53768 and R43-NS-38788, and the Department of Radiology, University of California, San Francisco. The authors thank Matthew Clay for the numerical simulations in Section 7.3.

Index Words

EEG, MEG, membrane, cable theory, synchrony, electromagnetism, source current, return current, volume conduction, multipole expansion, dipole, head model, conductivity, boundary conditions, lead field, half-sensitivity volume, data recording, reference electrode, average reference, spline interpolation, surface Laplacian, spatial filter.

References

Arfken GB, Weber HJ (1995) *Mathematical Methods for Physicists.* Academic Press.

Barnard ACL, Duck IM, Lynn MS, Timlake WP (1967a) The application of electromagnetic theory to electrocardiography: I. Derivation of integral equations. Biophysical Journal 7: 443–462.

Barnard ACL, Duck IM, Lynn MS, Timlake WP (1967b) The application of electromagnetic theory to electrocardiography: II. Numerical solution of the integral equations. Biophysical Journal 7: 463–491.

Barr RC, Ramsey M, Spach MS (1977) Relating epicardial to body surface potential distributions by means of transfer coefficients based on geometry measurements. IEEE Trans. on Biomed. Eng. 24: 1–11.

Baumann SB, Wonzy DR, Kelly SK, Meno FM (1997) The electrical conductivity of human cerebrospinal fluid at body temperature. IEEE Trans. on Biomed. Eng. 44(3): 220–223.

Braitenberg V, Schuz A (1991) *Anatomy of the Cortex: Statistics and Geometry.* Springer-Verlag.

Elul E (1972) The genesis of the EEG. Int. Rev. Neurobiol. 15: 227–272.

Ferree TC, Luu P, Russell GS, Tucker DM (2001) Scalp electrode impedance, infection risk, and EEG data quality. Clinical Neurophysiology 112:536–544.

Ferree TC (2006) Spherical splines and average referencing in scalp electroencephalography. *Brain Topography* 19(1-2): 43–52.

Foster KR, Schwan HP (1989) Dielectric properties of tissues and biological materials: A critical review. Critical Reviews in Biomed. Eng. 17(1): 25–104.

Geddes, L. A. and L. E. Baker (1967). The specific resistance of biological materials: A compendium of data for the biomedical engineer and physiologist. Med. Biol. Eng. 5: 271–293.

Geselowitz DB (1967) On bioelectric potentials in an inhomogeneous volume conductor. Biophysical Journal 7: 1–11.

Geselowitz DB (1998) The zero of potential. *IEEE Eng. Med. Biol. Mag.* 17(1): 128–132.

Gulrajani RM (1998) *Bioelectricity and Biomagnetism.* John Wiley and Sons.

Helmholtz HLF (1853) Ueber einige Gesetze der Vertheilung elektrischer Strome in korperlichen Leitern mit Anwendung auf die thierisch-elektrischen Versuche. Ann. Physik und Chemie 89: 211–233, 354–377.

Huhta JC, Webster JG (1973) 60-Hz interference in electrocardiography. IEEE Transactions on Biomedical Engineering 20: 91–101.

Jackson JD (1975) *Classical Electrodynamics.* John Wiley and Sons.

Koch C, Segev I (1989) *Methods in Neuronal Modeling: From Synapses to Networks.* MIT Press.

Law SK, Nunez PL, Wijesinghe RS (1993) High-resolution EEG using spline generated surface Laplacians on spherical and ellipsoidal surfaces. IEEE Transactions on Biomedical Engineering 40(2): 145–153.

Law SK (1993) Thickness and resistivity variations over the upper surface of the human skull. *Brain Topography* 6(2): 99–109.

Malmivuo J, Plonsey R (1995) *Bioelectromagnetism.* Oxford University Press.

Malmivuo J, Suihko V, Eskola H (1997) Sensitivity distributions of EEG and MEG measurements. IEEE Transactions on Biomedical Engineering 44(3): 196–208.

Makeig S, Westerfield M, Jung TP, Enghoff S, Townsend J, Courchesne E, Sejnowski TJ (2002) Dynamic brain sources of visual evoked responses. Science 295(5555): 690–4.

Nunez PL (1981) *Electric Fields of the Brain*. Oxford University Press.

Nunez PL (1995) *Neocortical Dynamics and Human EEG Rhythms*. Oxford University Press.

Nunez PL, Srinivasan R (2005) *Electric Fields of the Brain*. 2nd Edition, Oxford University Press.

Oostendorp TF, Delbeke J, Stegeman DF (2000) The conductivity of the human skull: Results from *in vivo* and *in vitro* measurements. IEEE Trans. on Biomed. Eng. 47(11): 1487–1492.

Perrin F, Pernier J, Bertrand O, Echallier JF (1989) Spherical splines for scalp potential and current density mapping. Electroencephalography and Clinical Neurophysiology 72: 184–187.

Perrin F, Pernier J, Bertrand O, Echallier JF (1990) Corrigenda: EEG 02274, Electroencephalography and Clinical Neurophysiology 76: 565.

Plonsey R (1969) *Bioelectric Phenomena.* Mc-Graw-Hill.

Plonsey R (1982) The nature of sources of bioelectric and biomagnetic fields. Biophys. J. 39: 309–312.

Press WH, Teukolsky SA, Vetterling WT, Flannery BP (1992) Numerical Recipes in C. Cambridge University Press.

Rush S, Driscoll DA (1968) Current distribution in the brain from surface electrodes. Anesthesia and analgesia 47(6): 717–723.

Rush S, Driscoll DA (1969) EEG electrode sensitivity – An application of reciprocity. IEEE Trans. on Biomed. Eng. 16(1): 15–22.

Schwan HP, Kay CF (1957) The conductivity of living tissues. Annals of New York Academy of Sciences 65: 1007.

Srinivasan R, Nunez PL, Tucker DM, Silberstein RB, Cadusch PJ (1996) Spatial sampling and filtering of EEG with spline Laplacians to estimate cortical potentials. Brain Topography 8(4): 355–366.

Srinivasan R, Tucker DM, Murias M (1998) Estimating the spatial Nyquist of the human EEG. Behavioral Research Methods, Instruments and Computers 30(1): 8–19.

Stok CJ (1987) The influence of model parameters on EEG-MEG single dipole source estimation. IEEE Trans. on Biomed Eng. 34(4): 289–296.

Zilles K (1990) Cortex. In: *The Human Nervous System* Pixinos G (ed.), Academic Press, New York.